Journal of Volcanology and Geothermal Research 427 (2022) 107551

Contents lists available at ScienceDirect

Journal of Volcanology and Geothermal Research

journal homepage: www.journals.elsevier.com/journal-of-volcanology-and-geothermal-research

High strain rate damage in porous andesite

Mai-Linh Doan [a,*], Michael J. Heap [b,c], Maude Schell [a], Ulrich Kueppers [d]

[a] Univ. Grenoble Alpes, Univ. Savoie Mont Blanc, CNRS, IRD, UGE, ISTerre, 38000 Grenoble, France
[b] Université de Strasbourg, CNRS, Institut Terre et Environnement de Strasbourg, UMR 7063, 5 rue René Descartes, Strasbourg F-67084, France
[c] Institut Universitaire de France (IUF), Paris, France
[d] Department of Earth and Environmental Sciences, Ludwig-Maximilians-Universität, 80333 Munich, Germany

ARTICLE INFO

Keywords:
High strain rate damage
Volcán de colima
Andesite
X-ray computed tomography
P-wave velocity
Split Hopkinson pressure bar

ABSTRACT

Deformation rates at volcanoes vary enormously, potentially altering the way in which volcanic rock accommodates strain. However, relationships between deformation rate, damage patterns, and physical properties are poorly understood. Laboratory deformation experiments are typically restricted to low strain rates ($< 1\ s^{-1}$). Here, we deformed samples of porous andesite in compression at strain rates from 10^{-6} to $\sim 370\ s^{-1}$ at room temperature. We show, using *X*-ray computed microtomography, that the failure mode changes as a function of strain rate: macroscopic fractures form at low strain rates and samples deformed at high strain rate ($\geq 100\ s^{-1}$) contain macroscopic fractures and collapsed pores. In general, high strain rate deformation results in more pervasively damaged samples. Deformation at high strain rate also results in larger decreases and increases to *P*-wave velocity and permeability, respectively. Strikingly, the change in the *P*-wave velocity of samples deformed at high strain rate is very large (decreases of up to 50%). We hypothesize that faster events (e.g., explosions) can shatter the adjacent host rock, which could destabilise the volcano and encourage mass wasting events, increase the efficiency of outgassing by increasing permeability, and increase the ash content of plumes that accompany Vulcanian explosions.

1. Introduction

Deformation rates at volcanoes vary tremendously, from 10^{-14}–$10^{-12}\ s^{-1}$ (Owen et al., 1995; Wadge et al., 2006; Moretti et al., 2020) to strain rates sufficient to fragment melt (Dingwell, 1996; Wadsworth et al., 2018) and form frictional melts (Kendrick et al., 2012; Hughes et al., 2020). However, the majority of laboratory deformation experiments on volcanic rocks have been performed at low compressive strain rates of $10^{-5}\ s^{-1}$ (Heap and Violay, 2021). Few experimental studies have focused on the strain rate dependence of mechanical behavior at higher strain rates up to $10^{-1}\ s^{-1}$ (Schaefer et al., 2015; Coats et al., 2018; Lavallée et al., 2019; Heap and Violay, 2021). These studies have shown that the strength of volcanic rocks increases as the strain rate is increased. For example, the strength of porous dacite from Mt. Unzen (Japan) increased from ~20 to ~28 MPa as the strain rate was increased from 10^{-5} to $10^{-1}\ s^{-1}$ (Coats et al., 2018).

Experiments on granite, marble, and porous sandstone have shown that rock can change failure mode at high strain rates (Aben et al., 2017a). Rather than forming the few macroscopic fractures observed at low strain rate ($\leq 10^{-1}\ s^{-1}$), very high strain rates ($\geq 100\ s^{-1}$) pulverize low-porosity granite (Doan and Gary, 2009) and marble (Doan and Billi, 2011) and compact porous sandstone (Aben et al., 2017b).

It is not clear, however, whether the failure mode of volcanic rock is similarly changed at high strain rates. For example, while Olsson (1991) remarked that the porous tuff samples were "reduced to dust" at strain rates of $10^3\ s^{-1}$, the failure of the low-porosity basalt was found to be largely independent of strain rate (Lindholm et al., 1974). Indeed, there are very few studies that have investigated the influence of high strain rates on the damage evolution and failure mode of volcanic rocks. Further, while studies exist that show that low strain rate deformation in the brittle regime ($\leq 10^{-1}\ s^{-1}$) can decrease *P*-wave velocities (Stanchits et al., 2006; Fortin et al., 2011) and increase permeability of volcanic rock (Fortin et al., 2011; Farquharson et al., 2016), corresponding data for high strain rates-important for the monitoring and understanding of volcanic systems-do not exist.

Here, we present the results of an experimental study on the influence of strain rate on the mechanical behavior of porous andesite. Room temperature uniaxial deformation experiments were performed at strain rates from 10^{-6} to $\sim 370\ s^{-1}$. The sample failure mode was assessed using *X*-ray computed microtomography (μCT), and the *P*-wave velocity

* Corresponding author.
E-mail address: Mai-linh.doan@univ-grenoble-alpes.fr (M.-L. Doan).

https://doi.org/10.1016/j.jvolgeores.2022.107551
Received 2 February 2022; Received in revised form 1 April 2022; Accepted 4 April 2022
Available online 7 April 2022

and permeability of select samples were measured before and after deformation. Finally, we outline the volcanological implications of these new data.

2. Materials and methods

2.1. Materials

The andesite block used for this study was collected from the lahar deposits in the "La Lumbre" valley on the southwest flank of Volcán de Colima (Mexico), a persistently-active andesitic stratovolcano located in the Trans-Mexican Volcanic Belt (Varley et al., 2019). The block is the same as that used in Farquharson et al. (2017). The andesite has a porphyritic texture that consists of a microlite-rich groundmass that hosts phenocrysts of plagioclase and pyroxene. The andesite contains irregularly-shaped pores and microcracks.

Cylindrical samples, 20 mm in diameter, were cored from the block and were cut and precision-ground to lengths of either 40 mm (for the "quasi-static" experiments) or 20 mm (for the "dynamic" experiments). The connected porosity of each sample was determined using the skeletal volume measured by a helium pycnometer (an AccuPyc II pycnometer manufactured by Micromeritics) and the bulk sample volume (Tab. 1). The isolated porosity of samples prepared from the same block of material was measured to be about 0.01 (Farquharson et al., 2017)

2.2. Low strain-rate testing

The low strain rate (from 10^{-6} to 10^{-3} s^{-1}) "quasi-static" experiments were performed at ITES (Strasbourg, France) using a uniaxial deformation apparatus manufactured by Schenck and modified in-house (see schematic provided in Heap et al., 2014). Experiments were performed on dry 40 mm-long samples at ambient laboratory temperatures. Axial displacement and axial force were measured by a linear variable differential transducer and a load cell, respectively. Axial displacement and axial force were converted to axial strain and axial stress using the sample dimensions.

2.3. High strain rate testing

The high strain rate "dynamic" experiments were performed using a Split Hopkinson Pressure Bar (SHPB) apparatus at ISTerre (Grenoble, France), which can impose uniaxial strain rates between 10 to 10^3 s^{-1} (Chen and Song, 2011; Gama et al., 2004). Experiments were performed on dry 20 mm-long samples at ambient laboratory pressures and temperatures. The sample is sandwiched between two long bars, one of which is impacted by a striker launched at several meters per second (Fig. 1a). Strain gauges on the bars quantify the stress wave loading the sample (Fig. 1b). Stress waves in elongated rod can be modelled as guided waves, the propagation of which can be predicted using the Pochhammer-Chree equation (Graff, 1991). The stress waves recorded in middle of the input bar and near the edge of the output bar can be

Table 1
Summary of the experimental results."Compacted/Fractured" damage is labeled as "C/F". Some data were not recorded and the corresponding cells are left blank.

	Sample	Dimensions (mm)		Porosity (%)	V_p (m/s)		Permeability (10^{-13} m^2)		Max Strain rate (/s)	Max strain (%)	Max stress (MPa)	Damage	
		Diameter	Height		Pre	Post	Pre	Post				Macroscopic	*X*-ray CT scan
SHPB	CLB1	20.06	20.47	18.23	3529	1712			196	1.13	42.6	C/F	C/F
	CLB2	20.09	20.21	18.23	4150	3853			58	0.38	31.5	Fractured	
	CLB3	20.07	17.63	19.22	3236	3181			121	0.5	16.7	Intact	
	CLB4	20.09	18.89	22.12	3072	1660			183	1.25	32.4	C/F	C/F
	CLB5	20.1	17.7	22.12	3106	1846			277	2.02	32.9	C/F	C/F
	CLB6	20.08	20.74	22.36	2861	2816			138	0.59	15.2	Intact	
	CLB7	20.07	19.72	21.31	2594	1814			259	1.58	37.7	C/F	C/F
	CLB8	20.09	19.54	17.76	2832				224	1.59	52.5	Fragmented	
	CLB9	20.08	18.61	20.49	2978	1505			369	3.23	30	C/F	C/F
	CLB10	20.11	20	18.86	3252	2967			201	0.78	36.8	C/F	C/F
	CLB11	20.1	20.53	22.01	2793	1251			213	2.56	32.8	C/F	C/F
	CLB12	20.12	18.78	21.2	2867	2834			57	0.51	25.1	Intact	Fractured
	CLB13	20.09	18.88	19.76	3120	2648			190	1.95	34.8	C/F	C/F
	CLB14	20.1	19.46	19.22	3050	2039			259	3	40.6	C/F	
	CLB15	20.1	20.32	20.96	3040	2239	9.31	27.1	171	1.63	34.1	C/F	C/F
	CLB16	20.05	21.6	22.99	2980				233	3.5	22.4	Fragmented	
	CLB17	20.11	20.12	17.37	2980	2668	2.76	6.22	153	0.79	38.6	Intact	C/F
	CLB18	20.13	18.34	18.91	3160	2810			67	0.58	30.7	Fractured	
	CLB20	20.12	19.16	21.99	3250	2798			125	1.38	24	C/F	
	CLB21	20.14	18.67	21.3	3120	2110			139	1.79	26	C/F	
Slow tests	LLB12	20.02	39.92	20.9			4.86	6.76	10^{-4}	0.74	26.6	Fractured	Fractured
	LLB15	20	39.75	24.15	2697	2583			10^{-5}	0.54	20.3	Fractured	
	LLB18	20	40.01	21.37					10^{-4}	0.81	29	Fractured	
	LLB19	20	39.99	21.07					10^{-3}	1.07	32.6	Fractured	
	LLB21	20.02	39.87	20.2	2820	2509			10^{-5}	0.49	31.9	Fractured	
	LLB22	19.99	39.68	21.65					10^{-6}	0.48	24.1	Fractured	Fractured
	LLB31	19.99	39.99	21.93					10^{-6}	0.46	22.9	Fractured	Fractured
	LLB34	20.02	40.01	22.23					10^{-3}	0.96	28.3	Fractured	
	LLB42	19.85	39.94	25.53	2656	2351			10^{-5}	0.44	18.3	Fractured	
	LLB44	20	40	20.87					10^{-5}	0.52	24.8	Fractured	
	LLB46	20	40	21.72					10^{-5}	0.51	22.5	Fractured	
	LLB48	19.88	39.95	26.76	2674	2579			10^{-5}	0.37	13.7	Fractured	
	LLB51	20	40	21.97					10^{-5}	0.51	20.6	Fractured	
	LLB52	20	40	22.4					10^{-5}	0.54	22.5	Fractured	
	LLB53	19.86	39.97	25.38	2807	2531			10^{-5}	0.39	15	Fractured	

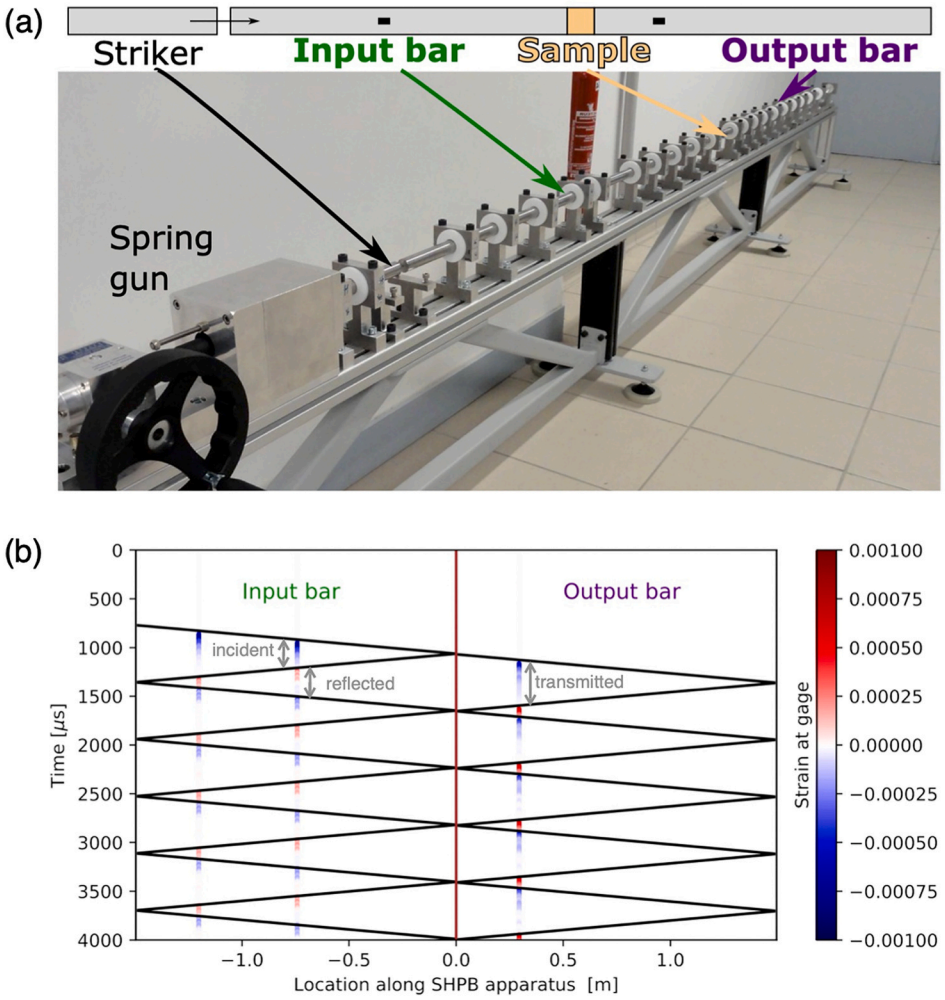

Fig. 1. Split Hopkinson Pressure bars (SHPB) at ISTerre (Grenoble, France). (a) Schematics of the SHPB device and relation for the samples. (b) The four strain gauges glued along the bars (at 120 cm and 74.4 cm from the right end of the input bar, and at 29.7 cm from the left end of the output bar) record the strain wave. The wave propagation can be also modeled using 1D stress propagation. Sample is at location 0.

estimated at the edges of the bars, and hence at the sample, to retrieve the first incident wave ε_i, the reflected wave ε_r, and the transmitted wave ε_t. Stresses and strain rates can then be computed as

$$\sigma_i = \frac{A_b}{A_s} E\,(\varepsilon_i + \varepsilon_r) \tag{1}$$

$$\sigma_o = \frac{A_b}{A_s} E\,\varepsilon_t \tag{2}$$

$$\frac{\partial \varepsilon}{\partial t} = \frac{c}{L}(\varepsilon_i - \varepsilon_r - \varepsilon_t) \tag{3}$$

where E, c are the Young modulus and the elastic bar wave speed of the bar material, respectively, and A_b and A_s are the cross-sectional area of the bar and the sample, respectively. The stresses at the input edge (σ_i) and at the output edge (σ_o) are compared to check the stress equilibrium of the sample during loading, which can be altered for strain rates or samples that are too high or too long, respectively. Once this quality control has been performed, the output stress is chosen as the stress acting on the sample during the test. Strain is computed by time integrating the strain rate. Full stress-strain curves can then be reliably retrieved (gray curves on Fig. 2).

After the first loading, the stress waves reflect perfectly at the edges of both bars: the bars have free edges and the sample is not reloaded. The stress-strain curves of the first loading reflects the whole loading history on the sample. By varying the striker length, the striker speed, the pulse shaper, and the material of the bars, a range of strain rates and stresses can be achieved.

2.4. X-ray imaging

X-ray imaging was performed at ISTerre on select samples before and after deformation. Damage patterns were assessed in two stages. In a first stage, the deformed samples were inspected visually. The samples were classified as either (1) intact, (2) fractured, (3) fractured with apparent compaction, and (4) macroscopically fragmented. In a second stage, the microstructure of select samples was investigated using μCT to provide 3D volumes with a voxel resolution of 15.8 μm. Following the μCT scans, we refined our damage classifications. A sample was classified as "fractured" when only macroscopic fractures were visible. When some compaction was visible (pores infilled with fragments), the sample was classified as "fractured with apparent compaction".

2.5. P-wave velocity and permeability

Damage was also assessed using petrophysical data. The *P*-wave velocity and permeability of select samples (deformed at low and high strain rates) was measured at ITES before and after deformation using a digital oscilloscope and a waveform pulse generator (see schematic provided in Heap et al., 2014) and a benchtop nitrogen permeameter (see schematic provided in Heap and Kennedy, 2016), respectively. Both

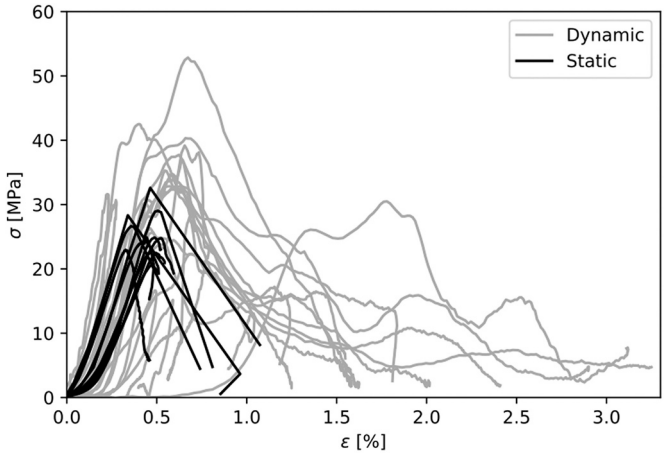

Fig. 2. Strain-stress curves for andesite deformed quasi-statically (10^{-6} to 10^{-3} s^{-1}; black curves) and dynamically (up to ~370 s^{-1}; gray curves).

P-wave velocity and permeability were measured parallel to the sample axis and at ambient laboratory temperatures. Volumetric flow rates were measured for different pressure differentials to calculate permeability using Darcy's law and to check for Klinkenberg and Forchheimer corrections. Due to the high permeability of the studied andesite, a Forchheimer correction was applied in all cases. *P*-wave velocity was measured at ambient pressure and permeability was measured under a confining pressure of 1 MPa.

3. Results

3.1. Mechanical behavior at different strain rates

A total of 35 experiments were performed: 15 quasi-static and 20 dynamic experiments. The stress-strain curves for all experiments are provided in Fig. 2. The stress-strain curves for the quasi-static tests (black curves) are similar to those for porous volcanic rock deformed in uniaxial compression (Heap and Violay, 2021). There are no qualitative differences between the stress-strain curves at strain rates between 10^{-6} to 10^{-3} s^{-1}. The stress-strain curves for the dynamic tests are similar to those for the quasi-static tests, although the samples deformed dynamically were typically deformed to larger strains (axial strains up to 3%, compared to 0.5–1% for the quasi-static tests, see Fig. 4b).

Fig. 3 shows the peak stress as a function of porosity for all samples (if the sample failed, the peak stress is equivalent to the uniaxial compressive strength). The strain rate of the quasi-static experiments is also indicated on Fig. 3. The peak stress of the samples deformed quasi-statically decreases as a function of increasing porosity, from ~33 MPa at a porosity of ~20% to ~13 MPa at a porosity of ~26.5%. The relationship between peak stress and porosity is similar for the samples deformed dynamically: peak stress decreases from 53 MPa at a porosity of 18% to 20 MPa at a porosity of 22.5%. Our data extend the findings of Heap and Violay (2021) and show that porosity exerts a first-order control on the uniaxial compressive strength of the studied andesite, at all strain rates (Fig. 3).

For a similar initial porosity (20–22%), although the strength at low-strain-rate (blue squares in Fig. 3) is lower than the strength at high strain rate (colored circles in Fig. 3), the influence of strain rate on strength plays a second order role compared to porosity. An increase of strength as a function of increasing strain rate has been previously observed in low (Schaefer et al., 2015; Coats et al., 2018; Lavallée et al., 2019; Heap and Violay, 2021) and high (Lindholm et al., 1974; Olsson, 1991) strain rate experiments on volcanic rocks, and it is typically explained in terms of the time available for subcritical crack growth processes (Heap et al., 2011). However, potential differences in fracture patterns have not been considered so far, and are discussed below.

3.2. Damage at different strain rates

The damage classification for each sample is presented in Fig. 4a, which shows that the type of damage depends on the strain rate. All of the quasi-statically deformed samples (10^{-6} and 10^{-3} s^{-1}) formed a macroscopic fracture, a failure mode that characterizes brittle deformation. However, apparent compaction occurred in addition to fracturing at strain rates above 120 s^{-1} and, at the highest strain rates, two of the samples macroscopically fragmented. μCT images of an intact sample, of a sample deformed quasi-statically, and of three samples deformed dynamically to different axial strains are shown in Fig. 5. The microstructure of the undeformed sample is complex, containing irregularly shaped and heterogeneously distributed pores (as shown in 3D

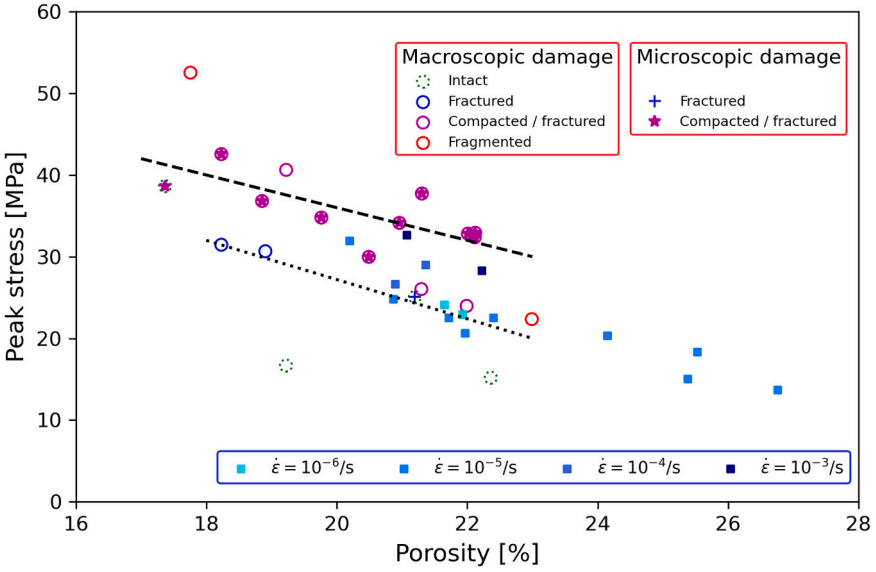

Fig. 3. Influence of porosity on the peak stress of porous andesite deformed over a wide range of strain rate (10^{-6} to ~370 s^{-1}). The squares represent the quasi-static experiments, and the circles represent the dynamic experiments. The damage classification for the samples tested at high strain rate was determined in two phases (visual macroscopic inspection and optional μCT imaging). All samples tested at low strain rate were fractured. Errors on the porosity and peak stress are <1%.

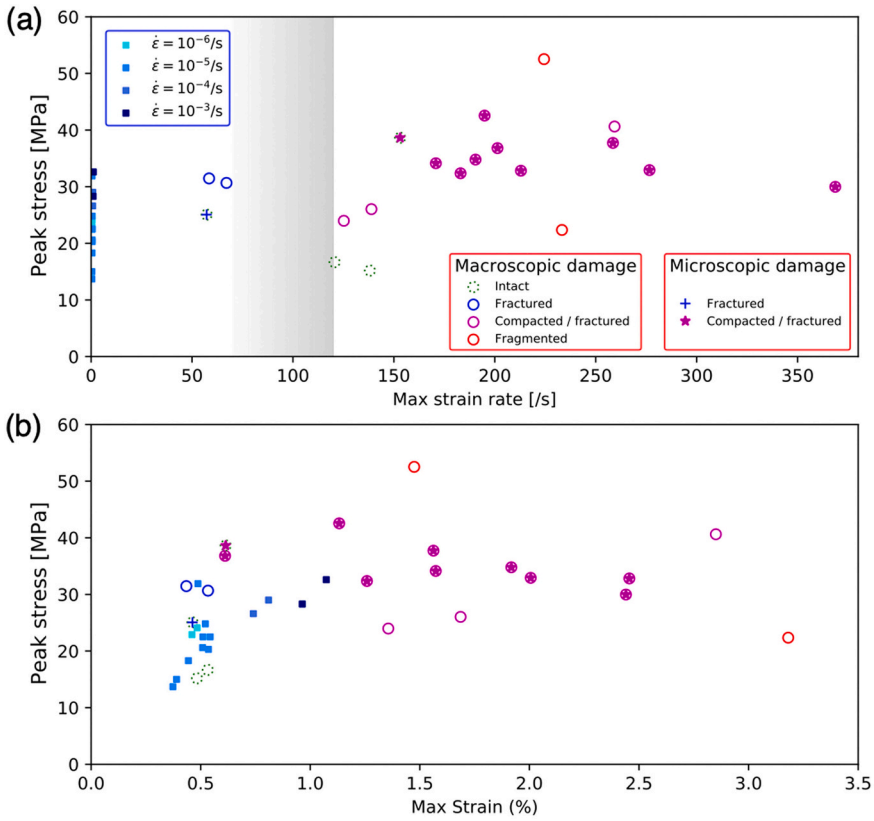

Fig. 4. Influence of strain and strain-rate (panels a and b) on the peak stress of porous andesite deformed over a wide range of strain rate (10^{-6} to ~370 s^{-1}). The squares represent the quasi-static experiments, and the circles represent the dynamic experiments. The damage classification for the samples tested at high strain rate was determined in two phases (visual macroscopic inspection and optional μCT imaging). All samples tested at low strain rate were fractured. Gray shade delimits the strain rate transition between fractured samples and compacted/fractured samples. Error on the peak stress is <1% and errors on the strain and strain rate are <5%.

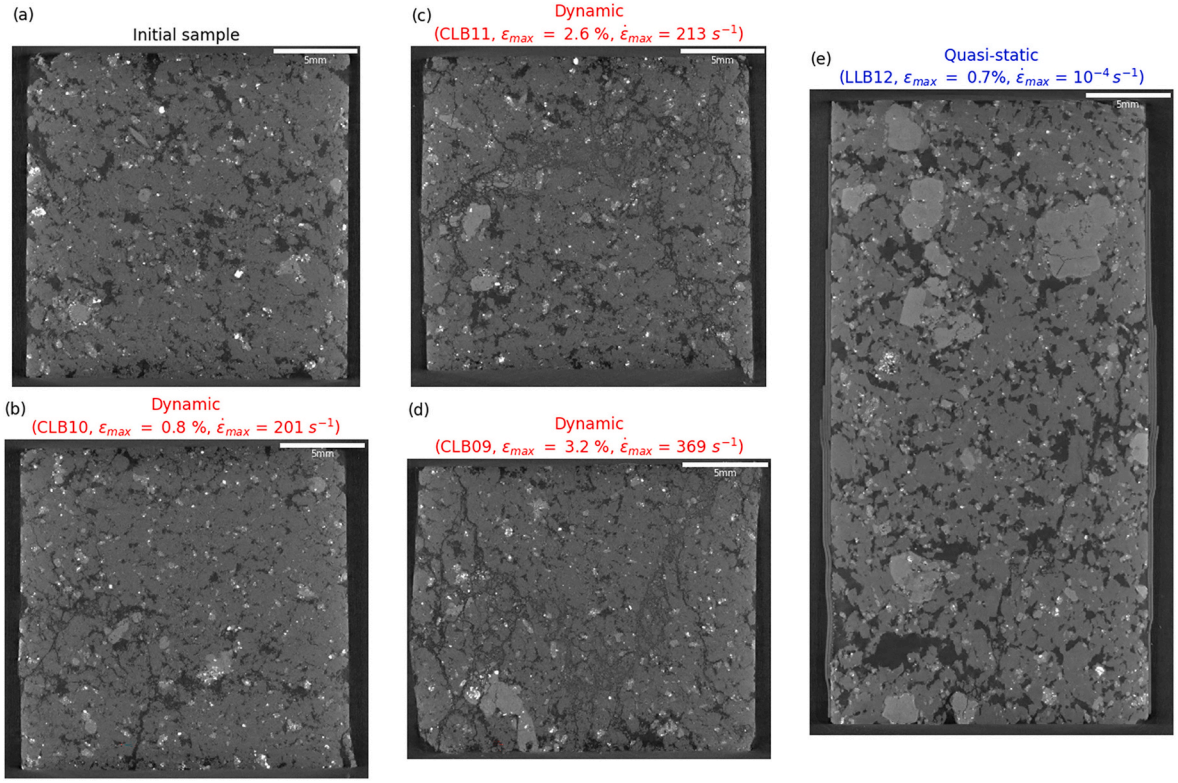

Fig. 5. X-ray computed tomographic slices (black and gray represent the porosity and rock, respectively) showing an intact sample (a) of the studied andesite and the failure modes at high (b–d) and low (e) strain rate.

μCT reconstructions of a similar andesite in Heap et al., 2020).

The quasi-statically deformed sample contains a macroscopic fracture, which extends from the middle of the sample on the right-hand-side to the bottom of the sample in the middle (Fig. 5e). The deformation is very localized in the quasi-statically deformed sample and little or no damage is observed outside the macroscopic fracture.

The damage accumulated in the sample dynamically deformed to a very similar axial strain is very different to the quasi-statically deformed sample (Fig. 5b). There is no macroscopic fracture, although some axially orientated fractures are present (e.g., at the bottom of the sample in the middle) and the large pores are now absent. The pores subsisting within the sample are infilled with fragments. Further, pore collapse in the sample deformed dynamically to an axial strain of 0.8% appears to be localized on a plane sub-perpendicular to the maximum principal stress, similar to the compaction bands seen previously to develop in porous volcanic rocks (Heap et al., 2015, 2020). The damage accumulated in the samples deformed dynamically to higher axial strains (2.6 and 3.2%) is similar to that described for the quasi-static sample to an axial strain of 0.8%, but much more pervasive (Figs. 5c and 5d).

Samples characterised by both fracturing and compaction have a higher strength than those that simply fractured (Fig. 3). This can be explained by the higher fracture energy required to accommodate microfracturing and grain crushing (Doan and D'Hour, 2012). To verify this, we have plotted the dissipated energy $\int_0^{\infty} \sigma(t) \frac{\partial \varepsilon(t)}{\partial t}$ dt as a function of the maximum strain experienced by a sample during loading (Fig. 6). These data show that the samples affected by the additional compaction dissipate more energy than the samples that only endured fracturing. Since the latter type of damage only occurs above 120 s^{-1}, it offers an explanation as to why most high strain rate samples exhibit higher values of strength.

3.3. Change in petrophysical properties at different strain rates

Fig. 7 shows the relative *P*-wave velocity decrease as a function of porosity, strain rate, strain, and dissipated energy. The *P*-wave velocity decrease does not depend on the initial sample porosity (Fig. 7a), but increases as a function of increasing strain rate (Fig. 7b). *P*-wave velocity decrease is $\leq$ 10% for the low strain samples (Fig. 7c), which also dissipated more energy (Figs. 6 and 7d). But the *P*-wave velocity decrease can exceed 50% at high strain (Fig. 7). It should be noted that such strains could only be achieved for the damage pattern "compacted/fractured", which is the most diffuse and occurs only for the dynamic tests (Fig. 4).

The pre- and post-deformation permeability was also measured for samples deformed at a strain rates of 10^{-4}, 49, and 171 s^{-1}, respectively, and showed a positive correlation of permeability increase with strain rate (Tab. 1). The increase in permeability following deformation is therefore higher (increase of about a factor of three) for the dynamic tests than for the quasi-static tests (increase of about 40%).

4. Discussion and implications

4.1. Change in failure mode at higher strain rates

Our data show samples accommodate strain differently at strain rates above 100 – 150 s^{-1}, from "fractured" to "fractured with apparent compaction" (Fig. 5). The occurrence of compaction bands"planes of collapsed pores connected by microcracks that formed sub-perpendicular to the maximum principal stress" has been observed during high-pressure quasi-static deformation experiments on porous andesites (Heap et al., 2015, 2020). Typically, effective pressures of 30–40 MPa would be required to form compaction bands in andesite with a similar porosity to the andesite studied here (Heap et al., 2015). Dynamic loading is known to induce a dynamic confinement effect, but the confining pressures generated are typically on the order of 5 MPa (Forrestal et al., 2007) and cannot therefore explain the presence of pore collapse during our dynamic tests (Fig. 5). Aben et al. (2017b) showed that compaction was also observed in porous sandstone deformed dynamically. These authors provided modeling to explain how the competition between intragranular fracturing (i.e. grain crushing) and intergranular fracture is resolved by kinetic effects. The stress intensity factor increases as the axial stress increases, and fracturing can occur when the stress intensity factor is greater than the fracture toughness, which is sensitive to stress rate (Bhat et al., 2012). This threshold stress occurs earlier in the deformation process for intragranular processes, but at higher stresses. Intergranular fracturing (i.e. macroscopic fracture formation) is therefore favored thermodynamically but is inhibited kinetically, explaining why compaction can occur at higher strain rates under uniaxial conditions (Aben et al., 2017b).

4.2. Changes in petrophysical properties

Our study has shown that changes to permeability and *P*-wave velocity following macroscopic failure are larger at higher strain rates

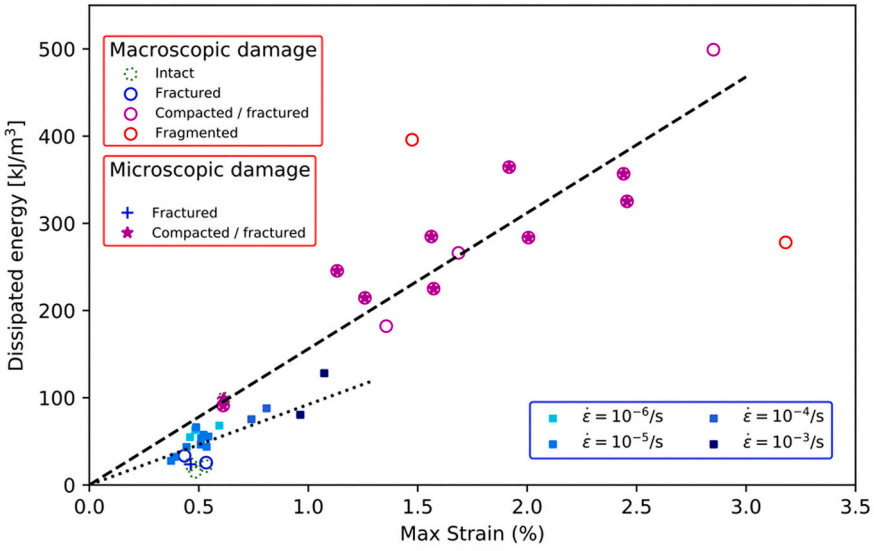

Fig. 6. Increase of dissipated energy during loading as a function of strain. The samples that experience compaction/fracturing dissipate more energy than the samples who just endured fracturing. Errors are <5%.

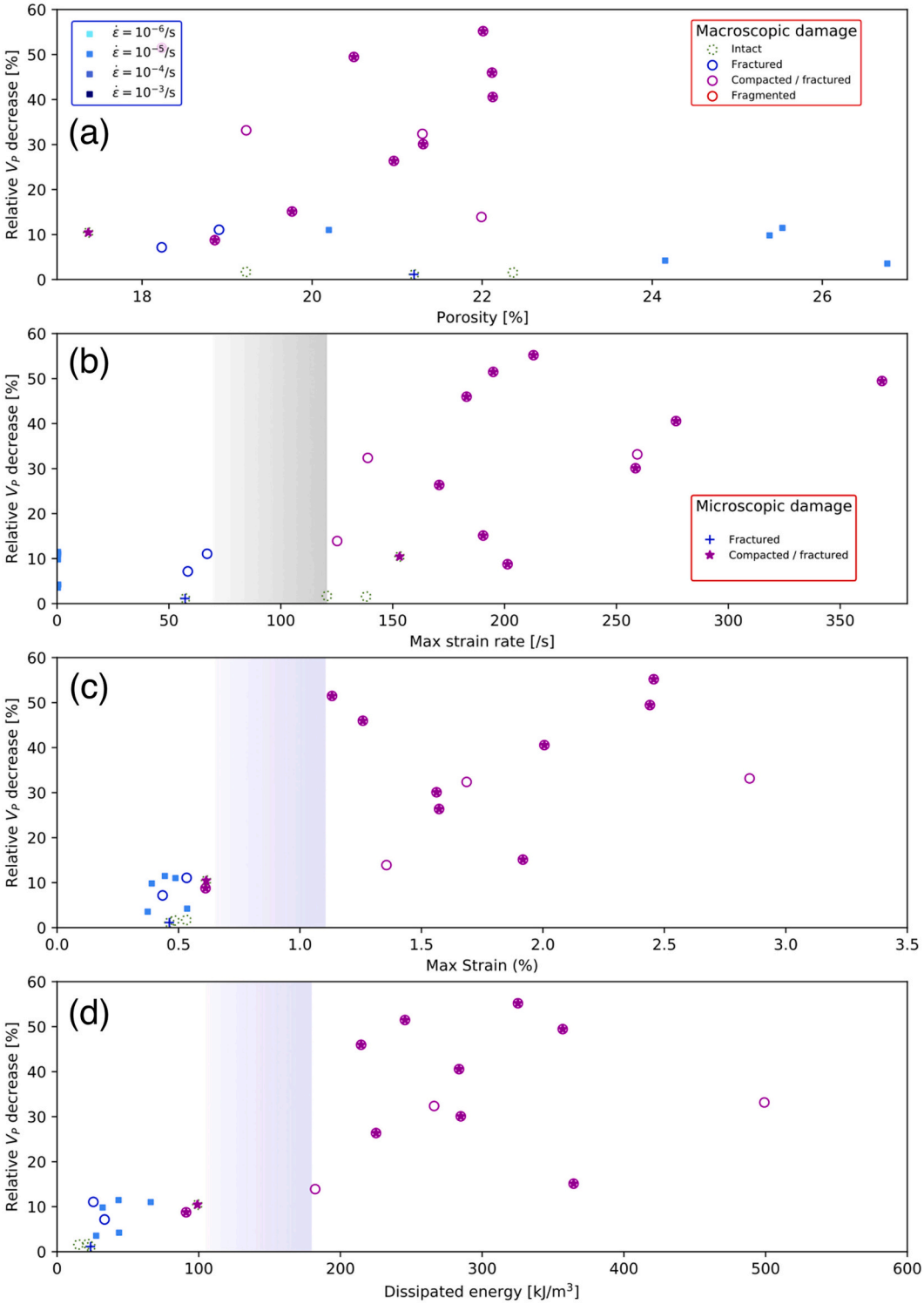

Fig. 7. Relative change in *P* wave velocity as a function of (a) porosity, (b) strain rate, (c) strain, (d) dissipated energy. The squares represent the quasi-static experiments, and the circles represent the dynamic experiments. Errors on the *P*-wave velocity and porosity are <1%, all other errors are <5%.

(Table 1; Fig. 7). Previous studies have shown that brittle failure in compression increases the permeability of volcanic rock (Fortin et al., 2011; Heap et al., 2015; Farquharson et al., 2016), and that cataclastic pore collapse decreases the permeability of volcanic rock (Heap et al., 2015, 2020; Farquharson et al., 2017). Our data show, however, that the permeability of samples deformed at high strain rates that are "fractured with apparent compaction" increased by about a factor of three (Table 1). In other words, the observed compaction (pores infilled with fragments and possible compaction bands; Fig. 5) did not result in a decrease in permeability and is likely the result of presence of axially orientated fractures (Fig. 5), not present in samples deformed quasi-statically at high pressure (Heap et al., 2015, 2020; Farquharson et al., 2017). The larger increase in permeability with increasing strain rate is likely the result of the more pervasive damage in the samples deformed at high strain rates (Fig. 5).

A decrease in *P*-wave velocity following quasi-static loading to

failure (Fig. 7) has been observed previously in volcanic rocks and is due to the formation of dilatant microcracks (Stanchits et al., 2006; Fortin et al., 2011). The very large decrease in *P*-wave velocity (a decrease of up to 50%) following dynamic loading to failure, not observed previously, is likely consequence of the pervasively damaged and fragmented nature of the samples deformed at high strain rate (Fig. 5). A decrease of 50% is higher than previously recorded reductions in *P*-wave velocity associated with high strain rate damage. For crystalline rocks, Aben et al. (2015) recorded *P*-wave velocity reductions up to 30% for the diffuse fracturing associated with high strain rate damage. Rempe et al. (2013) showed through subsurface seismic studies that velocities in pulverized zones of the San Andreas Fault Zone (USA) can be as low as 1 km/s, a reduction to 20% of the expected values for the granitic protolith.

4.3. Volcanological implications of intense high strain rate damage

The decrease in *P*-wave velocities after high-strain-rate loading is spectacular, especially considering they were obtained on laboratory samples, which tend to have higher *P*-wave velocities than those observed in the field (Lesage et al., 2018b). Although our porous andesite samples were not pulverized at high strain rates (as was the case for low-porosity granites; Doan and Gary, 2009), the significant decrease in *P*-wave velocity (Fig. 7) and the pervasively damaged and fragmented nature of the samples deformed at high strain rate (Fig. 5), suggests that high strain rate damage will result in a permanent decohesion that could severely weaken the rock units of the volcanic edifice or the magma, both inside the conduit and above (e.g., the lava dome). Although our dynamic experiments were performed at room temperature, we consider that our results are relevant for magma at depth that can locally respond in a brittle way to high strain rates (Dingwell, 1996). Therefore, we anticipate that high strain rate damage at depth will texturally resemble the observed microstructures in our post-mortem samples (Fig. 5). However, evidence may well be eventually erased if a combination of magma glass transition temperature, continued deformation, and time allow for the particles to viscously sinter (Wadsworth et al., 2014).

Field measurements at Volcán de Colima show that the center of the volcano exhibits similar decrease in seismic velocity at the kilometric scale, extending down to 30 km (Escudero and Bandy, 2017). A decrease in *P*-wave velocity is sometimes attributed to an increase in temperature, due to the decrease in elastic wave velocities associated with thermal cracking (Vinciguerra et al., 2005; Nara et al., 2011), and may indicate the presence of magma. At Volcán de Colima, however, the velocity change is more intense and wider in the shallow subsurface. We hypothesize that a combination of repeated addition of magma into the volcanic edifice, several related heating and cooling cycles, as well as the seismic energy imparted during fracture opening (i.e. local) and explosive eruptions (i.e. entire edifice), resulted in considerable volumes of weakened material at Volcán de Colima, and also at other frequently-active stratovolcanoes worldwide. Indeed, Lesage et al. (2014) found that the velocity of shallow layers of the volcano could change as the waves generated by earthquakes pass through them.

Such weakened volcanic rock will respond differently to subsequent deformation episodes (at any deformation rate) and could (1) mask pre-eruption deformation (which was difficult to discern before the 2015 eruption at Volcán de Colima; Lesage et al., 2018a), (2) destabilize the volcanic edifice and promote mass wasting events (Voight and Elsworth, 1997; Borselli et al., 2011) and associated hazards, (3) increase the efficiency of outgassing by increasing permeability (Lavallée et al., 2013; Farquharson et al., 2015), and (4) increase the ash content of eruption plumes of explosive eruptions (Webb et al., 2014). Indeed, fragments of shattered host rock ('lithics') may be readily incorporated into the gas-particle jet of a subsequent high-energy explosive eruption. Finally, increasing the permeability (Table 1) and the surface area available for fluid-rock interactions (Fig. 5) could encourage efficient hydrothermal alteration, a process that could also further reduce the stability of the volcanic flank or lava dome (Heap et al., 2021).

Declaration of Competing Interest

Mai-Linh Doan reports financial support was provided by Université Grenoble Alpes (Vulnérabilités des Ouvrages aux Risques). Michael Heap reports financial support was provided by French Universities Institute.

Acknowledgements

M. Heap acknowledges support from the Institut Universitaire de France (IUF). T. Reuschlé and B. Renaudie are thanked for experimental assistance. N. Varley and J. Farquharson are thanked for their help in collecting the experimental material. The comments of Phil Benson and one anonymous reviewer helped improve this manuscript.

References

Aben, F.M., Doan, M., Gratier, J.P., Renard, F., 2017a. Coseismic damage generation and pulverization in fault zones: insights from dynamic Split-Hopkinson pressure bar experiments. Geophys. Monogr. 227, 47–80. https://doi.org/10.1002/9781119156895.ch4.

Aben, F.M., Doan, M.L., Gratier, J.P., Renard, F., 2017b. High strain rate deformation of porous sandstone and the asymmetry of earthquake damage in shallow fault zones. Earth Planet. Sci. Lett. 463, 81–91. https://doi.org/10.1016/j.epsl.2017.01.016.

Aben, F.M., Doan, M.L., Mitchell, T.M., Toussaint, R., Reuschlé, T., Fondriest, M., Gratier, J.P., Renard, F., 2015. Dynamic fracturing by successive coseismic loadings leads to pulverization in active fault zones. J. Geophys. Res. Solid Earth 121 (121), 2338–2360. https://doi.org/10.1002/2015JB012542.

Bhat, H.S., Rosakis, A.J., Sammis, C.G., 2012. A micromechanics based constitutive model for brittle failure at high strain rates. J. Appl. Mech. Trans. ASME 79. https://doi.org/10.1115/1.4005897.

Borselli, L., Capra, L., Sarocchi, D., De la Cruz-Reyna, S., 2011. Flank collapse scenarios at Volcán de Colima, Mexico: a relative instability analysis. J. Volcanol. Geotherm. Res. 208, 51–65. https://doi.org/10.1016/j.jvolgeores.2011.08.004.

Chen, W.W., Song, B., 2011. Split Hopkinson (Kolsky) Bars. Design Testing and Applications. First edit. Springer, New York. https://doi.org/10.1007/978-1-4419-7982-7.

Coats, R., Kendrick, J.E., Wallace, P.A., Miwa, T., Hornby, A.J., Ashworth, J.D., Matsushima, T., Lavallée, Y., 2018. Failure criteria for porous dome rocks and lavas: a study of Mt. Unzen. Jpn. Solid Earth 9, 1299–1328. https://doi.org/10.5194/se-9-1299-2018.

Dingwell, D.B., 1996. Volcanic dilemma: flow or blow ? Science 273, 1054–1055.

Doan, M., Billi, A., 2011. High strain rate damage of carrara marble. Geophys. Res. Lett. 38 https://doi.org/10.1029/2011GL049169.

Doan, M., D'Hour, V., 2012. Effect of initial damage on rock pulverization along faults. J. Struct. Geol. 45, 113–124. https://doi.org/10.1016/j.jsg.2012.05.006.

Doan, M., Gary, G., 2009. Rock pulverization at high strain rate near the San Andreas fault. Nat. Geosci. 2, 709–712. https://doi.org/10.1038/ngeo640.

Escudero, C.R., Bandy, W.L., 2017. Ambient seismic noise tomography of the Colima volcano complex. Bull. Volcanol. 79 https://doi.org/10.1007/s00445-016-1096-2.

Farquharson, J., Heap, M.J., Varley, N.R., Baud, P., Reuschlé, T., 2015. Permeability and porosity relationships of edifice-forming andesites: a combined field and laboratory study. J. Volcanol. Geotherm. Res. 297, 52–68.

Farquharson, J.I., Baud, P., Heap, M.J., 2017. Inelastic compaction and permeability evolution in volcanic rock. Solid Earth 8, 561–581.

Farquharson, J.I., Heap, M.J., Baud, P., 2016. Strain-induced permeability increase in volcanic rock. Geophys. Res. Lett. 43, 11,603–11,610. https://doi.org/10.1002/2016GL071540.

Forrestal, M.J., Wright, T.J., Chen, W.W., 2007. The effect of radial inertia on brittle samples during the Split-Hopkinson pressure bar test. Int. J. Impact Eng. 34, 405–411. https://doi.org/10.1016/j.ijimpeng.2005.12.001.

Fortin, J., Stanchits, S., Vinciguerra, S., Guéguen, Y., 2011. Influence of thermal and mechanical cracks on permeability and elastic wave velocities in a basalt from mt. etna volcano subjected to elevated pressure. Tectonophysics 503, 60–74.

Gama, B.A., Lopatnikov, S.L., Gillespie, J.W., 2004. Hopkinson bar experimental technique: a critical review. Appl. Mech. Rev. 57, 223. https://doi.org/10.1115/1.1704626.

Graff, K.F., 1991. Wave Motion in Elastic Solids. Dover Publications, New York.

Heap, M., Lavallée, Y., Petrakova, L., Baud, P., Reuschle, T., Varley, N., Dingwell, D.B., 2014. Microstructural controls on the physical and mechanical properties of edifice-forming andesites at volcán de colima, mexico. J. Geophys. Res. Solid Earth 119, 2925–2963.

Heap, M.J., Baud, P., McBeck, J.A., Renard, F., Carbillet, L., Hall, S.A., 2020. Imaging strain localisation in porous andesite using digital volume correlation. J. Volcanol. Geotherm. Res. 404, 107038. https://doi.org/10.1016/j.jvolgeores.2020.107038.

Heap, M.J., Baud, P., Meredith, P.G., Vinciguerra, S., Bell, A.F., Main, I.G., 2011. Brittle creep in basalt and its application to time-dependent volcano deformation. Earth Planet. Sci. Lett. 307, 71–82. https://doi.org/10.1016/j.epsl.2011.04.035.

Heap, M.J., Baumann, T.S., Rosas-Carbajal, M., Komorowski, J.C., Gilg, H.A., Villeneuve, M., Moretti, R., Baud, P., Carbillet, L., Harnett, C., et al., 2021. Alteration-induced volcano instability at la soufrière de guadeloupe (eastern caribbean). J. Geophys. Res. Solid Earth 126 e2021JB022514.

Heap, M.J., Farquharson, J., Baud, P., Lavallée, Y., Reuschlé, T., 2015. Fracture and compaction of andesite in a volcanic edifice. Bull. Volcanol. 77 https://doi.org/10.1007/s00445-015-0938-7.

Heap, M.J., Kennedy, B.M., 2016. Exploring the scale-dependent permeability of fractured andesite. Earth Planet. Sci. Lett. 447, 139–150.

Heap, M.J., Violay, M.E., 2021. The mechanical behaviour and failure modes of volcanic rocks: a review. Bull. Volcanol. 83 https://doi.org/10.1007/s00445-021-01447-2.

Hughes, A., Kendrick, J.E., Salas, G., Wallace, P.A., Legros, F., Di Toro, G., Lavallee, Y., 2020. Shear localisation, strain partitioning and frictional melting in a debris avalanche generated by volcanic flank collapse. J. Struct. Geol. 140, 104132.

Kendrick, J.E., Lavallée, Y., Ferk, A., Perugini, D., Leonhardt, R., Dingwell, D.B., 2012. Extreme frictional processes in the volcanic conduit of mount st. helens (usa) during the 2004-2008 eruption. J. Struct. Geol. 38, 61–76. https://doi.org/10.1016/j.jsg.2011.10.003.

Lavallée, Y., Benson, P.M., Heap, M.J., Hess, K.U., Flaws, A., Schillinger, B., Meredith, P. G., Dingwell, D.B., 2013. Reconstructing magma failure and the degassing network of dome-building eruptions. Geology 41, 515–518.

Lavallée, Y., Heap, M.J., Kendrick, J.E., Kueppers, U., Dingwell, D.B., 2019. The fragility of volcán de colima-a material constraint. In: Varley, N.R., Connor, C.B., Komorowski, J.C. (Eds.), Volcán de Colima. Springer, pp. 241–266. https://doi.org/10.1007/978-3-642-25911-17.

Lesage, P., Carrara, A., Pinel, V., Arámbula-Mendoza, R., 2018a. Absence of detectable precursory deformation and velocity variation before the large dome collapse of July 2015 at Volcán de Colima. Mexico. Front. Earth Sci. 6, 1–12. https://doi.org/10.3389/feart.2018.00093.

Lesage, P., Heap, M.J., Kushnir, A., 2018b. A generic model for the shallow velocity structure of volcanoes. J. Volcanol. Geotherm. Res. 356, 114–126. https://doi.org/10.1016/j.jvolgeores.2018.03.003.

Lesage, P., Reyes-Dávila, G., Arámbula-Mendoza, R., 2014. Large tectonic earthquakes induce sharp temporary decreases in seismic velocity in Volcán de Colima, Mexico. J. Geophys. Res. Solid Earth 119, 4360–4376. https://doi.org/10.1002/2013JB010884.

Lindholm, U.S., Yeakley, L.M., Nagy, A., 1974. The dynamic strength and fracture properties of dresser basalt. Int. J. Rock Mechan. Min. Sci. 11, 181–191. https://doi.org/10.1016/0148-9062(74)90885-7.

Moretti, R., Komorowski, J.C., Ucciani, G., Moune, S., Jessop, D., de Chabalier, J.B., Beauducel, F., Bonifacie, M., Burtin, A., Vallée, M., Deroussi, S., Robert, V., Gibert, D., Didier, T., Kitou, T., Feuillet, N., Allard, P., Tamburello, G., Shreve, T., Saurel, J.M., Lemarchand, A., Rosas-Carbajal, M., Agrinier, P., Le Friant, A., Chaussidon, M., 2020. The 2018 unrest phase at La Soufrière of Guadeloupe (French West Indies) andesitic volcano: scrutiny of a failed but prodromal phreatic eruption. J. Volcanol. Geotherm. Res. 393, 106769. https://doi.org/10.1016/j.jvolgeores.2020.106769.

Nara, Y., Meredith, P.G., Yoneda, T., Kaneko, K., 2011. Influence of macro-fractures and micro-fractures on permeability and elastic wave velocities in basalt at elevated pressure. Tectonophysics 503, 52–59.

Olsson, W.A., 1991. The compressive strength of tuff as a function of strain rate from 10^{-6} to 10^{3}/s. Int. J. Rock Mechan. Min. Sci. 28, 115–118. https://doi.org/10.1016/0148-9062(91)93241-W.

Owen, S.E., Segall, P., Freymueller, J., Mikijus, A., Denlinger, R., Arnadóttir, T., Sako, M., Bürgmann, R., 1995. Rapid deformation of the south flank of kilauea volcano Hawaii. Science 267, 1328–1332. https://doi.org/10.1126/science.267.5202.1328.

Rempe, M., Mitchell, T.M., Renner, J., Nippress, S., Ben-Zion, Y., Rockwell, T.K., 2013. Damage and seismic velocity structure of pulverized rocks near the San Andreas Fault. J. Geophys. Res. Solid Earth 118, 2813–2831. https://doi.org/10.1002/jgrb.50184.

Schaefer, L.N., Kendrick, J.E., Oommen, T., Lavallée, Y., Chigna, G., 2015. Geomechanical rock properties of a basaltic volcano. Front. Earth Sci. 3, 1–15. https://doi.org/10.3389/feart.2015.00029.

Stanchits, S., Vinciguerra, S., Dresen, G., 2006. Ultrasonic velocities, acoustic emission characteristics and crack damage of basalt and granite. Pure Appl. Geophys. 163, 974–993. https://doi.org/10.1007/s00024-006-0059-5.

Varley, N.R., Connor, C.B., Komorowski, J.C., 2019. Volcán de Colima. Springer, Heidelberg. https://doi.org/10.1007/978-3-642-25911-1.

Vinciguerra, S., Trovato, C., Meredith, P.G., Benson, P.M., 2005. Relating seismic velocities, thermal cracking and permeability in mt. etna and iceland basalts. Int. J. Rock Mechan. Min. Sci. 42, 900–910.

Voight, B., Elsworth, D., 1997. Failure of volcano slopes. Geotechnique 47, 1–31.

Wadge, G., Mattioli, G.S., Herd, R.A., 2006. Ground deformation at Soufrière Hills Volcano, Montserrat during 1998-2000 measured by radar interferometry and GPS. J. Volcanol. Geotherm. Res. 152, 157–173. https://doi.org/10.1016/j.jvolgeores.2005.11.007.

Wadsworth, F.B., Vasseur, J., von Aulock, F.W., Hess, K.U., Scheu, B., Lavallée, Y., Dingwell, D.B., 2014. Nonisothermal viscous sintering of volcanic ash. J. Geophys. Res. Solid Earth 119, 8792–8804.

Wadsworth, F.B., Witcher, T., Vossen, C.E., Hess, K.U., Unwin, H.E., Scheu, B., Castro, J. M., Dingwell, D.B., 2018. Combined effusive-explosive silicic volcanism straddles the multiphase viscous-to-brittle transition. Nat. Commun. 9, 1–8.

Webb, E.B., Varley, N.R., Pyle, D.M., Mather, T.A., 2014. Thermal imaging and analysis of short-lived Vulcanian explosions at Volcán de Colima, Mexico. J. Volcanol. Geotherm. Res. 278–279. https://doi.org/10.1016/j.jvolgeores.2014.03.013, 132-145.